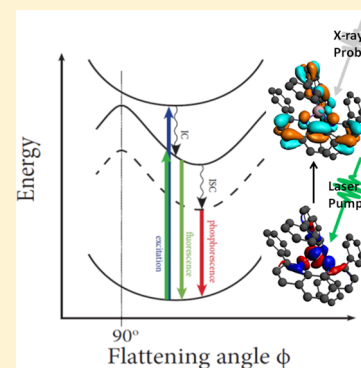


Effects of Electronic and Nuclear Interactions on the Excited-State Properties and Structural Dynamics of Copper(I) Diimine Complexes

Michael W. Mara,^{†,‡} Nicholas E. Jackson,^{†,‡} Jier Huang,[‡] Andrew B. Stickrath,[‡] Xiaoyi Zhang,[§] Nosheen A. Gothard,[†] Mark A. Ratner,[†] and Lin X. Chen^{†,‡,*}[†]Department of Chemistry, Northwestern University, 2145 Sheridan Road, Evanston, Illinois 60208-3113, United States[‡]Chemical Sciences and Engineering Division and [§]X-ray Science Division of the Advanced Photon Source, Argonne National Laboratory, 9700 South Cass Avenue, Argonne, Illinois 60439, United States

Supporting Information

ABSTRACT: The effects of structural constraints on the metal-to-ligand charge transfer (MLCT) excited state structural dynamics of cuprous bis-2,9-diphenyl-phenanthroline ($[\text{Cu}(\text{I})(\text{dpp})_2]^+$) in both coordinating acetonitrile and noncoordinating toluene were studied using X-ray transient absorption (XTA) spectroscopy and density functional theory (DFT) calculations. The phenyl groups attached to the phenanthroline ligands not only effectively shield the Cu(I) center from solvent molecules, but also force a flattened tetrahedral coordination geometry of the Cu(I) center. Consequently, the MLCT state lifetime in $[\text{Cu}(\text{I})(\text{dpp})_2]^+$ is solvent-independent, unlike the previously studied 2,9-methyl substituted bis-phenanthroline Cu(I) complex. The MLCT state of $[\text{Cu}(\text{I})(\text{dpp})_2]^+$ still undergoes a “pseudo Jahn–Teller distortion,” with the angle between the two phenanthroline ligand planes decreased further by 7° . The XTA results indicate that, in the MLCT excited state of $[\text{Cu}(\text{I})(\text{dpp})_2]^+$, the phenyls at the 2, 9 positions of the phenanthroline rotate, breaking the π – π interaction with the phenanthroline ligands without ever rotating in-plane with the phenanthroline ligands. Hence, the transferred electron density from the Cu(I) center is localized on the phenanthroline moiety with no charge density present on the phenyl rings. The insight about the effect of the structural constraints on the MLCT state properties will guide the design of Cu(I) diimine complexes with suitable excited-state properties to function as earth-abundant dye sensitizers for solar electricity generation.



1. INTRODUCTION

The photoexcited states of transition metal complexes have played key roles in processes and devices converting solar energy to fuels and electricity, such as in photocatalysts and dye-sensitized solar cells (DSSCs).^{1–3} Cu(I) diimine complexes have many properties similar to those of the ruthenium polypyridyl complexes commonly used as photocatalysts and light sensitizers in solar fuel and electricity production.^{2,4–15} As in the ruthenium polypyridyl complexes, Cu(I) diimine complexes can donate electrons from the metal center to the imine ligands in the metal-to-ligand charge transfer (MLCT) excited state, and their visible absorption mirrors those of the ruthenium complexes. As a much cheaper alternative to ruthenium dyes, copper-based dyes have the potential to turn DSSCs into considerably more practical and marketable solar energy conversion devices. However, there are still major concerns regarding the use of Cu diimine complexes, including the lability of the photogenerated Cu(II) center,^{16,17} significant Jahn–Teller distortions in the excited state, heavily structure-dependent energetics,¹⁸ low oxidation potential,^{17,19} and the generation of nonradiative “exciplexes,” with much shorter MLCT state lifetimes in coordinating solvents.^{4,20} The question then is if these issues can be addressed by tuning the structures of these complexes to make the excited-state properties suitable

for their intended functions. To achieve this goal, we need to understand the environment-dependent excited-state properties of these complexes, such as the MLCT state lifetimes, intersystem crossing (ISC) rates, and electron/energy transfer yields, and how these processes correlate with the structural reorganization in the MLCT state.

The photophysical properties of the copper(I) *bis*-2,9-dimethylphenanthroline ($[\text{Cu}(\text{I})(\text{dmp})_2]^+$) complex have been extensively investigated.^{4,16,20–28} In the ground state, $[\text{Cu}(\text{I})(\text{dmp})_2]^+$ adopts a pseudo tetrahedral coordination with D_{2d} symmetry. The lowest energy visible absorption bands of $[\text{Cu}(\text{I})(\text{dmp})_2]^+$ correspond to MLCT transitions; upon excitation, one of the d electrons of the copper is transferred to the phenanthroline ligands, converting the copper center from a Cu(I) $3d^{10}$ to a Cu(II) $3d^9$ configuration. The now asymmetrically occupied copper center undergoes a second-order, pseudo Jahn–Teller distortion, causing the molecule to flatten into a D_2 geometry, which decreases the angle between the two phenanthroline ligand planes. Since the Cu(II) center prefers a 5-coordinate geometry, either solute or a solvent

Received: November 26, 2012

Revised: January 12, 2013

Published: January 16, 2013

molecule can bind to the copper center, generating a nonradiative “exciplex” that lowers the overall energy of the complex and hence decreases the excited-state lifetime due to the energy gap law.^{4,29} Quantum mechanical calculations have shown that the spin–orbit coupling (SOC) in this system is a function of the angle between the two phenanthroline ligand planes; increased flattening will decrease SOC and thus slow down the ISC rate while lowering the total energy of the system. Thus, the design of efficient copper-based sensitizer dyes is a delicate balance among these factors.

On the basis of these studies, two important structural factors are recognized to be influential to the MLCT state properties: the solvent accessibility to the copper center and the angle between the two phenanthroline planes. Much of the interest around copper phenanthrolines stems from the fact that their photophysical properties can be varied by changing the substituents at the 2 and 9 positions of the phenanthroline.^{5,11,25,28,30–33} While the unsubstituted Cu(I) bisphenanthroline, [Cu(phen)₂]⁺, exhibits almost no emission and has a MLCT state lifetime as short as a few picoseconds, the 2,9 methyl-substituted [Cu(I)(dmp)₂]⁺ exhibits a higher emission quantum yield and a prolonged MLCT state lifetime of over 100 ns in noncoordinating solvents. [Cu(I)(dmp)₂]⁺ is arguably the most thoroughly investigated of the copper phenanthroline family by quantum mechanical calculations,^{18,34–36} transient optical spectroscopic measurements,^{18,37,38} and transient X-ray spectroscopic measurements.^{16,37,39} The excited-state dynamics have been well described: upon excitation to the ¹MLCT state, [Cu(I)(dmp)₂]⁺ experiences a subpicosecond pseudo Jahn–Teller distortion,^{16,18} converting the molecule to a D₂ symmetry and extending the ISC time constant to ~10–20 ps. From here, there are only two significant pathways available: either the complex can phosphoresce on the nanosecond time scale, or it can form an exciplex with a solvent molecule and quickly undergo nonradiative decay. X-ray transient absorption (XTA) measurements have shown that these exciplexes can be formed both in coordinating solvents, such as acetonitrile, or in noncoordinating solvents, such as toluene.³⁷

There are two primary methods for modulating the properties of copper phenanthrolines by varying the substituents at the 2,9 positions of phenanthroline: (1) increase the bulkiness of the alkyl groups, such as adding *tert*-butyl groups to effectively hinder the flattening and solvent access,⁴⁰ or (2) adding aryl groups to flatten the pseudotetrahedral ground state geometry and provide longer wavelength absorption for light harvesting.^{33,41} [Cu(I)(dpp)₂]⁺, with phenyl substituents at the 2 and 9 positions of the phenanthroline, exhibits drastically different ground and excited-state properties than [Cu(I)(dmp)₂]⁺. Crystal structures show that [Cu(I)(dpp)₂]⁺ adopts a rather flattened and distorted ground-state geometry, resulting in a broader absorption spectrum with a red shoulder extending out to nearly 700 nm.⁴² Furthermore, this complex exhibits a longer lifetime than [Cu(I)(dmp)₂]⁺ and is much more resistant to coordinating solvents, maintaining a high emission quantum yield even in coordinating solvents such as acetonitrile.¹⁶ While the solvent resistance of the MLCT state lifetime for these complexes is encouraging, the origin for this property and the excited-state structural dynamics for these complexes still remain relatively unknown.

XTA spectroscopy measurements have proven useful in the determination of both the electronic and structural properties of excited states of many transition metal complexes, including

[Cu(I)(dmp)₂]⁺.^{37,39} XTA is essentially the X-ray equivalent of optical transient absorption (TA) spectroscopy. XTA measurements can simultaneously yield both the electronic density of a specific atom and the local structure surrounding that atom with a resolution of 0.01–0.02 Å. In this work, we present XTA measurements on [Cu(I)(dpp)₂]⁺ in both acetonitrile and toluene. The structure of photoexcited [Cu(I)(dpp)₂]⁺ (*[Cu(I)(dpp)₂]⁺) was determined via both XTA and DFT methods and compared to both [Cu(I)(dpp)₂]⁺ and the oxidized [Cu(II)(dpp)₂]²⁺. We will discuss the solvent dependency of [Cu(I)(dpp)₂]⁺. Finally, we will discuss the ramifications that these properties have on using phenyl-substituted copper phenanthrolines in solar-energy conversion devices.

2. EXPERIMENTAL, COMPUTATIONAL, AND ANALYSIS METHODS

2.1. XTA Measurements. The experimental setup for the XTA measurements at Beamline 11IDD of the Advanced Photon Source at Argonne National Laboratory has been described elsewhere.^{43–45} Briefly, a 527 nm, 5 ps laser pulse at 1 kHz repetition rate was obtained from the second harmonic of an Nd:YAG laser to excite a 4 mM [Cu(I)(dpp)₂]⁺ sample in acetonitrile. A 1 mM sample in toluene was analyzed in the same fashion. The laser power used was ~970 mW. The APS storage ring was operating in 24-bunch mode, where each X-ray bunch with width ~80–100 ps was separated by ~153.5 ns from other bunches in the storage ring. One of these bunches was synchronized with the laser pulse and was set to 100 ps after the laser pulse using a programmable delay generator (PDL-100A-20NS, Colby Instruments). HPLC tubing of length 10 cm was used to establish a fast laminar flow (a nozzle with a diameter of 0.7 mm, a flow rate of ~50 mL/min) which allows fresh sample volumes to be excited by consecutive laser pulses at 1 kHz repetition rate. The rest of the sample recirculation system consists of a closed loop of Teflon tubing driven by a peristaltic pump. As described earlier, X-ray fluorescence signals were collected by custom-built avalanche photodiode (APD) detectors. A Z-1 filter/soller slit combo was attached in front of each detector element with six absorption lengths of NiO Z-1 filter to remove most of the elastic scattering signal. A 25-μm thick black polyimide film was placed in front of the Z-1 filter to protect it and block scattered laser light from reaching the APD detectors. The APD outputs were connected to two fast analyzer cards (Agilent), where signals from all pulses in the X-ray pulse train were individually digitized. The pulse shape, signal offset, and dark counts were recorded and used for an *in situ* curve fitting procedure (G. Jennings). Forty scans were collected over the course of 20 h per sample; there were ~250 points per scan with 4 s integration per point. The XANES region of each scan was monitored for any signs of sample degradation. Monochromator glitches and top-up corrections were performed using a third APD upstream of the sample, which collected a small portion of X-ray scattering that was divided out of the raw data.

2.2. XAFS Data Analysis. XAFS data analysis was performed using the FEFF and IFEFFIT packages.⁴⁶ Programs Athena and Artemis were used for data preprocessing and fitting, respectively.⁴⁷ All scans were calibrated using a Cu foil as a reference, with the edge energy set as the peak of the first derivative. Background subtraction was performed using Athena's Autobk algorithm, using a *k*-weight of 2 and an *R*_{bkg} value of 0.7. *R*_{bkg} is an upper limit on the low-*R* region over

which the *R*-space XAFS data is fit, and is related to the number of knots in the spline according to the equation:

$$N_{\text{knots}} = \frac{2R_{\text{bkg}}\Delta k}{\pi} \quad (1)$$

where Δk is the range of usable data in the spectrum.⁴⁸ The XANES spectrum of with the laser excitation was fit to a linear combination of the ground state spectra for Cu(I) and Cu(II) species using a linear combination analysis algorithm in the Athena program. (See the Supporting Information.) The estimated value of 75% ground state was obtained and its contribution to the spectrum after the laser excitation taken within 100 ps was then removed, yielding the 100% excited-state XAFS spectrum.

The copper K-edge X-ray absorption fine structure (XAFS) spectra provide information on the local structure surrounding the copper center. The oscillatory XAFS signals are caused by the interference between the outgoing photoelectron wave originating from the copper center and the backscattered photoelectron waves from the surrounding atoms.^{49–51} Hence, the Fourier transform of this interference pattern yields a pseudo radial distribution function centered about the Cu atoms. By fitting a theoretical model to the experimental data, the structural parameters corresponding to the structure of the complex can be extracted from the following equation:^{49–52}

$$\chi(k) = \sum_i \frac{F_{\text{eff}}(k)S_0^2(k)N_i}{kR_i^2} \exp^{-2k^2\sigma_i^2} \sin[2kR_i + \phi_i(k)] \quad (2)$$

where *i* is the index for neighboring shells around the X-ray absorbing atom (e.g., Cu at Cu K-edge here), $F_{\text{eff}}(k)$ is the magnitude of the backscattering, S_0^2 , the amplitude reduction factor, N_i the number of atoms in the *i*th neighboring shell and R_i the corresponding average distance, σ_i^2 the Debye–Waller factor or mean-squared displacement, and ϕ_i the phase shift; and *k* the photoelectron wavevector.

All experimental XAFS data were processed and analyzed by the program Artemis^{46,47} for fitting in *R*-space. A previously published crystal structure of $[\text{Cu(II)(dpp)}_2]^+$ was used as the model structure for all systems,⁴² and all of the scattering paths were generated using the FEFF 6.0 program built in to Artemis. The same S_0^2 and ΔE parameters were used for all fits in each data set, and the same scattering paths were used in the multishell fits for each sample. Multiple scattering contributions were found to be mostly insignificant, except at rather high *R*, where Cu–C–Cu scattering paths were included.

2.3. DFT Calculations. Calculations were performed using the ADF2010.02 suite of programs.^{53–55} The B3LYP hybrid-exchange functional with a zeroth order regular approximation (ZORA)^{56–58} scalar relativistic correction was used for the modeling of the $[\text{Cu(I)(dpp)}_2]^+$ complex. A double- ζ polarized (DZP) basis set was used for the description of C, N, and H atoms, and a triple- ζ polarized (TZP) basis set was used to describe the atomic orbitals of copper. $[\text{Cu(I)(dpp)}_2]^+$ restricted and $[\text{Cu(II)(dpp)}_2]^{2+}$ unrestricted ground state geometry optimizations were performed under a D_2 symmetry constraint, and normal-mode analysis (positive eigenvalues of the Hessian matrix) confirmed that converged geometries were true energy minima. Long-range dispersion effects were included to accurately model phenyl-phenanthroline π – π stacking interactions, and were taken into account with the Grimme empirical dispersion correction.⁵⁹ Vertical singlet and

triplet excitation energies calculated at the optimized ground-state geometry were performed using time-dependent density functional theory (TDDFT).⁶⁰ Excited-state geometries of the lowest-lying triplet states were relaxed using an unrestricted B3LYP geometry optimization under D_2 symmetry.

3. RESULTS

3.1. UV–vis Spectra. The ground-state absorption spectrum of $[\text{Cu(I)(dpp)}_2]^+$ (Figure 1) displays two strong

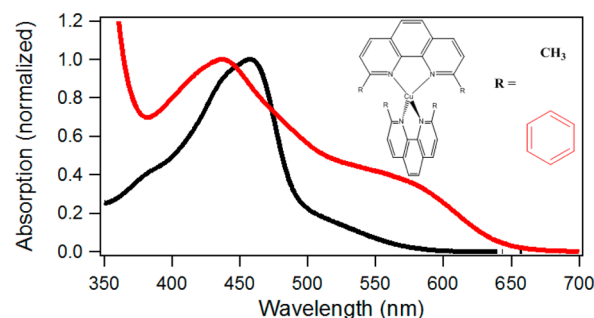


Figure 1. UV–vis spectrum of $[\text{Cu(I)(dpp)}_2]^+$ (red). Absorption spectrum of $[\text{Cu(I)(dmp)}_2]^+$ (black) is shown for comparison. The molecular structures of both molecules are shown on the right.

absorption features, a peak at 435 nm and a broad shoulder above 500 nm, both corresponding to MLCT transitions.⁶¹ On the basis of our previous studies of Cu(I) diimine complexes with different groups at the 2 and 9 positions of phenanthroline ligands,^{24,40} the shoulder feature is due to the MLCT transition from the flattened pseudotetrahedral geometry. Hence, the strong absorption shoulder feature indicates that $[\text{Cu(I)(dpp)}_2]^+$ has a flattened pseudotetrahedral geometry, while the ground state of $[\text{Cu(I)(dmp)}_2]^+$ exists in a nearly tetrahedral geometry, indicated by a much weaker shoulder feature.^{34,62,42} This flattened coordination geometry in the ground state is also evidenced through XANES spectral features (see below).

3.2. XANES and XAFS Spectra. The Cu K-edge XANES spectra of $[\text{Cu(I)(dpp)}_2]^+$, $^*[\text{Cu(I)(dpp)}_2]^+$, and $[\text{Cu(II)(dpp)}_2]^{2+}$ are shown in Figure 2. Similar to $[\text{Cu(I)(dmp)}_2]^+$, $[\text{Cu(I)(dpp)}_2]^{2+}$ also exhibits a strong peak feature at 8.986 keV assigned to a $1s \rightarrow 4p_z$ transition.^{63,64} The intensity of this band is strongly linked to the angle between the two

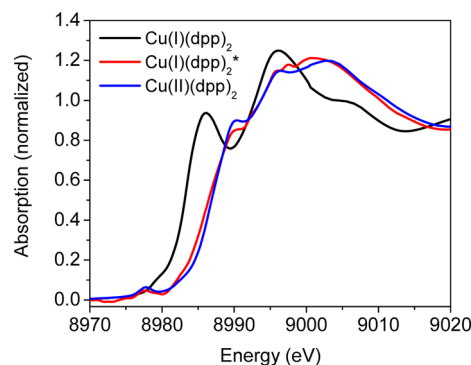


Figure 2. XANES spectra of $[\text{Cu(I)(dpp)}_2]^+$, $^*[\text{Cu(I)(dpp)}_2]^+$, and $[\text{Cu(II)(dpp)}_2]^{2+}$. Measurements taken at Cu K-edge; $^*[\text{Cu(I)(dpp)}_2]^+$ was excited at 527 nm. All samples were ~4 mM in acetonitrile.

phenanthroline ligand planes,⁶³ as the delocalization caused by the flattening process will reduce the $3d-4p$ mixing, depopulating the electron density in the $4p_z$ orbital due to the mixing and hence increasing the intensity of this transition. The X-ray crystal measurements show that the Cu(I) center in $[\text{Cu(I)(dpp)}_2]^+$ adopts a flattened tetrahedral coordination geometry in the ground state so that the phenyl groups can π -stack with the opposite phenanthroline ligand, which is further supported by the observed XANES spectra. It is interesting to note that both $[\text{Cu(II)(dpp)}_2]^{2+}$ and photogenerated $^*[\text{Cu(I)(dpp)}_2]^+$ have the $1s \rightarrow 4p_z$ transition shifted to 8.990 keV from that of the ground state $[\text{Cu(I)(dpp)}_2]^+$. This, along with a newly emerged pre-edge $1s \rightarrow 3d$ transition peak at 8.978 keV upon the laser excitation, suggest a Cu(II) center in the MLCT state because only Cu(II) with a $3d^9$ configuration can give a rise of the $1s \rightarrow 3d$ pre-edge feature.

The XANES spectra of both $^*[\text{Cu(I)(dpp)}_2]^+$ and $[\text{Cu(II)(dpp)}_2]^{2+}$ in Figure 2 show an apparent relative edge shift of ~ 3 eV, associated with the oxidation of the Cu(I) center. Using the distinctly different XANES features for the ground state and the MLCT state approximated by the spectrum of $[\text{Cu(II)(dpp)}_2]^{2+}$, in particular the $1s \rightarrow 4p_z$ peak, the XTA spectrum after the laser excitation was reconstructed from a linear combination of the ground and MLCT state spectra. The resulting spectrum agreed well with the experimental spectrum, from which we determined that the fraction of the MLCT state population in the laser excited sample was $\sim 25\%$. This value is determined by fitting the spectrum as a linear combination of the $[\text{Cu(I)(dpp)}_2]^+$ and $[\text{Cu(II)(dpp)}_2]^{2+}$ spectra over a range of -20 to 30 eV with respect to the absorption edge (see the Supporting Information).

The flattening of the pseudotetrahedral coordination geometry of the copper center will only enhance the intensity of the $1s \rightarrow 4p_z$ peak, while the oxidation of Cu(I) center will shift the peak to a higher energy. Thus, the apparent depletion from its position in the ground state spectrum holds dynamic structural information regarding the Cu(I) oxidation and coordination geometry changes. Therefore, we measured the X-ray signal intensity at the characteristic $1s \rightarrow 4p_z$ peak position at 8.986 keV as a function of the time delay between the laser and X-ray pulses with the results shown in Figure 3. The instrument response time is ~ 80 ps (fwhm), the duration of X-ray bunches. The laser pulse delay scans indicate that the depletion of the $1s \rightarrow 4p_z$ peak due to the formation of the Cu(II) species is completed within the X-ray probe pulse

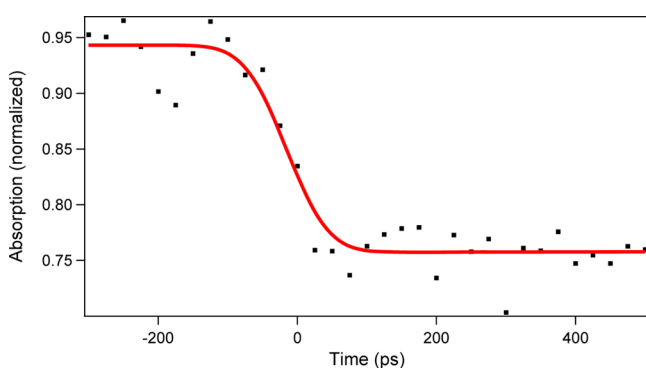


Figure 3. Laser delay scan at $[\text{Cu(I)(dpp)}_2]^+$ pre-edge peak, showing the depletion of the $1s \rightarrow 4p_z$ peak. Time resolution is ~ 80 – 100 ps, determined by the width of the X-ray bunch.

duration after excitation, as expected from our previous TA measurements on $[\text{Cu(I)(dpp)}_2]^+$ where the two fast time constants are sub-ps and ~ 10 ps.¹⁶ The only observable change in the signal intensity takes place within 100 ps delay and has a very long recovery time constant corresponding to the $^3\text{MLCT}$ excited state that decays with a time constant of ~ 100 ns in acetonitrile.¹⁶ Fluorescence upconversion and TA measurements of $[\text{Cu(I)(dmp)}_2]^+$ have shown that the Jahn–Teller flattening distortion is subpicosecond,^{16,18} while the ISC lifetime ranges from 10 to 20 ps; therefore, the 80-ps X-ray pulse from the synchrotron source is expected to be too long to see the structural evolution. The dynamics observed here for the depletion of the $1s \rightarrow 4p_z$ peak is consistent with the previous results.¹⁶

The XAFS spectra for $[\text{Cu(I)(dpp)}_2]^+$, $^*[\text{Cu(I)(dpp)}_2]^+$, and $[\text{Cu(II)(dpp)}_2]^{2+}$ in k -space and the magnitude and imaginary functions in R -space after Fourier transformation can be found in Figure 4; the fits, in magnitude and imaginary R space, can be found in Figure 5. The Fourier transforms of these XAFS spectra were all performed within $k = 2.6$ – 7.7 \AA^{-1} with a k^3 -weighting, and the fittings were carried out in the R -space within $R = 1$ – 3.4 \AA , using scattering paths calculated from the crystal structures by the FEFF program.^{46,65} The magnitude and imaginary FT spectra reveal relative shifts in the average Cu-to-atom distances in $^*[\text{Cu(I)(dpp)}_2]^+$ and $[\text{Cu(II)(dpp)}_2]^{2+}$ from those of $[\text{Cu(I)(dpp)}_2]^+$, while the imaginary spectrum reveals differences in peak position and magnitudes between the $^*[\text{Cu(I)(dpp)}_2]^+$ and the $[\text{Cu(II)(dpp)}_2]^{2+}$ in the 2–2.5 \AA region (Figure 5). The peaks in this region represent the Cu–C distances associated with eight C atoms of the phenanthroline connected directly to the four Cu-ligating N atoms (carbons (b) and (c)). Also, the first peak, corresponding to the Cu–N scattering path, for $^*[\text{Cu(I)(dpp)}_2]^+$ and $[\text{Cu(II)(dpp)}_2]^{2+}$ is shifted to lower R relative to that of $[\text{Cu(I)(dpp)}_2]^+$. The magnitude of this peak for $^*[\text{Cu(I)(dpp)}_2]^+$ is much higher than both $[\text{Cu(I)(dpp)}_2]^+$ and $[\text{Cu(II)(dpp)}_2]^{2+}$ which is likely due to its higher noise level in the raw data causing an exaggerated amplitude.

The results from the R -space fits of $[\text{Cu(I)(dpp)}_2]^+$, $^*[\text{Cu(I)(dpp)}_2]^+$, and $[\text{Cu(II)(dpp)}_2]^{2+}$ in acetonitrile can be found in Table 1 and were based on a $[\text{Cu(II)(dpp)}_2]^{2+}$ crystal structure (Scheme 1).⁴² The Cu–N distance in $^*[\text{Cu(I)(dpp)}_2]^+$ and $[\text{Cu(II)(dpp)}_2]^{2+}$ is shortened by 0.04 \AA relative to $[\text{Cu(I)(dpp)}_2]^+$ and has a smaller Debye–Waller factor than in the ground state, indicating a smaller distribution of Cu–N distances. The Cu–C(d) distance is 0.1 \AA higher in the ground state than in the photoexcited or oxidized species and is the most significant structural change observed between the separate species. This distance change is indicative of rotation of the phenyl ring and corresponds to $\sim 10^\circ$ rotation into the plane of the phenanthroline ligand, as shown by rotating the phenyl rings in the calculated $[\text{Cu(I)(dpp)}_2]^+$ by 10° into the plane of the phenanthroline. While it might be expected that the phenyl rings would fully rotate into the phenanthroline plane to establish conjugation between the two, it should be noted that the in-plane phenyl is expected to have a Cu–C(d) distance of $\sim 2.85 \text{ \AA}$, which is inconsistent with the obtained XAFS data. Furthermore, the hydrogen atom attached to C(d) would be left only $\sim 1.8 \text{ \AA}$ away from the copper center, so it seems unlikely that the phenyl could adopt this “planar” orientation due to a sterics argument. The ramifications of the phenyl-phenanthroline dihedral angle will be discussed later. Both $^*[\text{Cu(I)(dpp)}_2]^+$ and $[\text{Cu(II)(dpp)}_2]^{2+}$ exhibit comparable

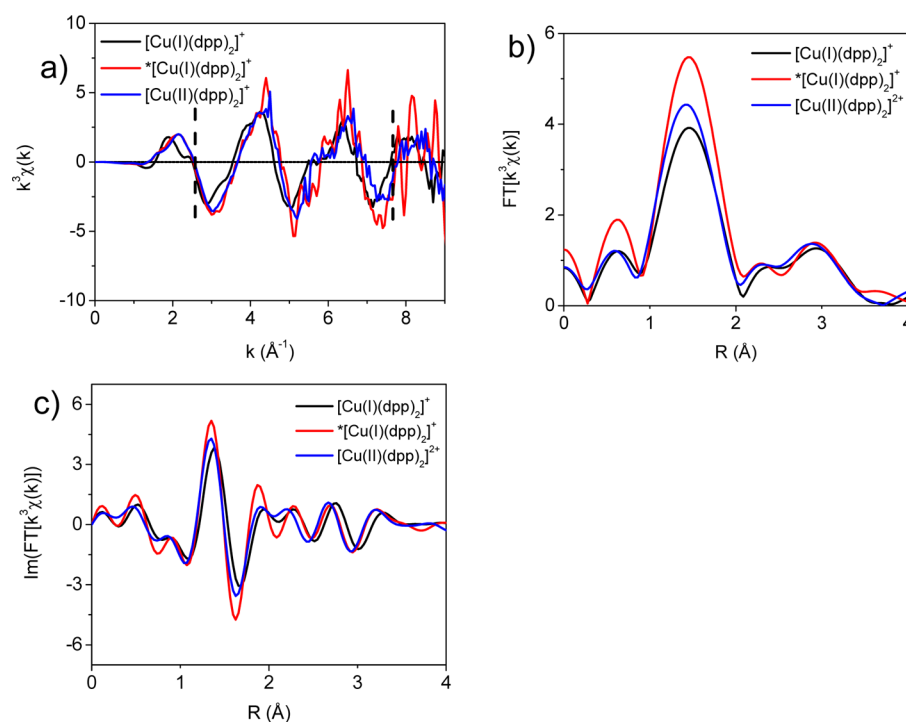


Figure 4. XAFS spectra of $[\text{Cu}(\text{I})(\text{dpp})_2]^+$, $*[\text{Cu}(\text{I})(\text{dpp})_2]^+$, and $[\text{Cu}(\text{II})(\text{dpp})_2]^{2+}$ in (a) k -space, (b) R -space, and (c) imaginary R -space in acetonitrile. Range of $2.6\text{--}7.7\text{ \AA}^{-1}$ was used for Fourier Transform (Hanning window, range shown by dotted lines in plot a).

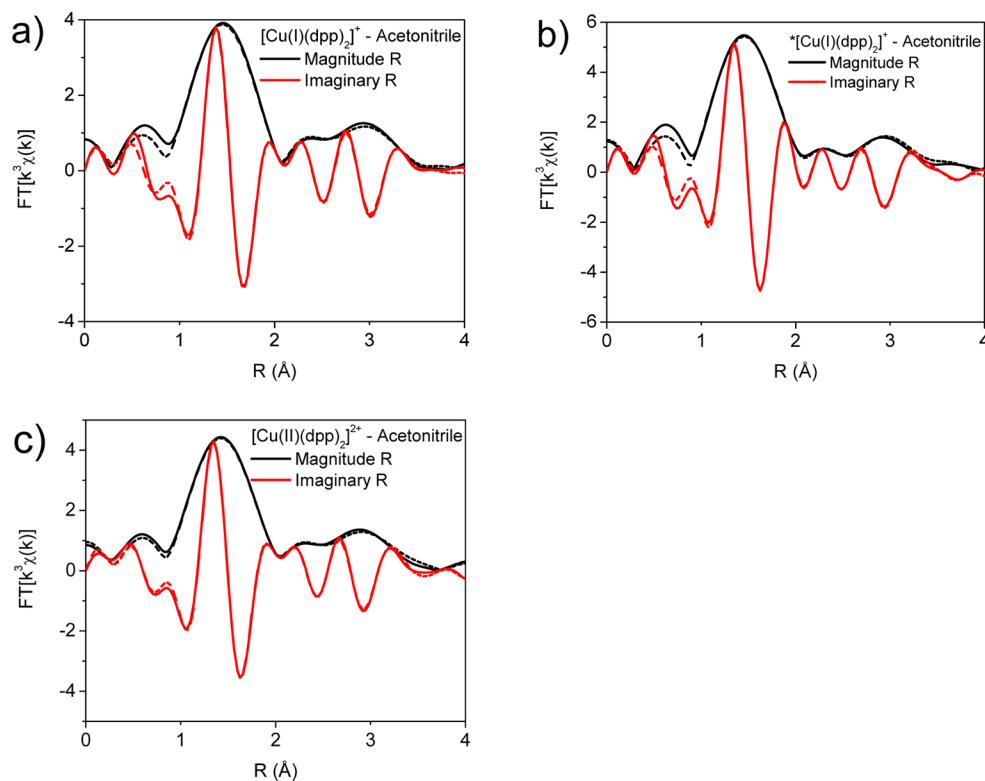


Figure 5. Fourier transform (solid) and best fit (dashed) for the following: (a) $[\text{Cu}(\text{I})(\text{dpp})_2]^+$, (b) $*[\text{Cu}(\text{I})(\text{dpp})_2]^+$, and (c) $[\text{Cu}(\text{II})(\text{dpp})_2]^{2+}$. Spectra were fit over an R range of $1\text{--}3.4\text{ \AA}$.

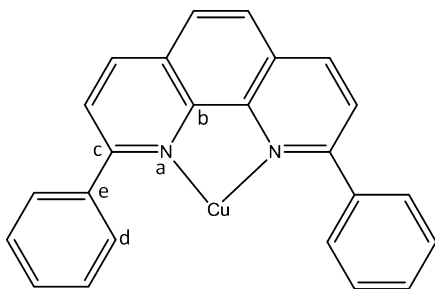
Cu–N and Cu–C distances within the experimental errors. More specifically, the Cu–N and Cu–C(d and e) paths in both species are indistinguishable within the XAFS structural resolution, while small differences are found in the Cu–C(a

and b) distances that coincide with the differences in the $2\text{--}2.5\text{ \AA}$ region of imaginary R -space spectra previously mentioned.

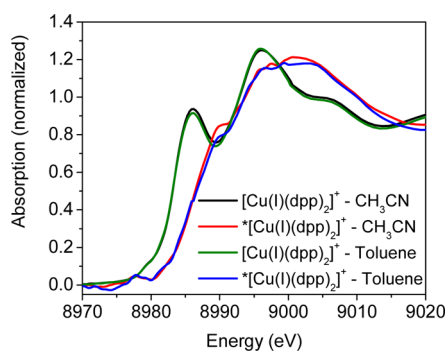
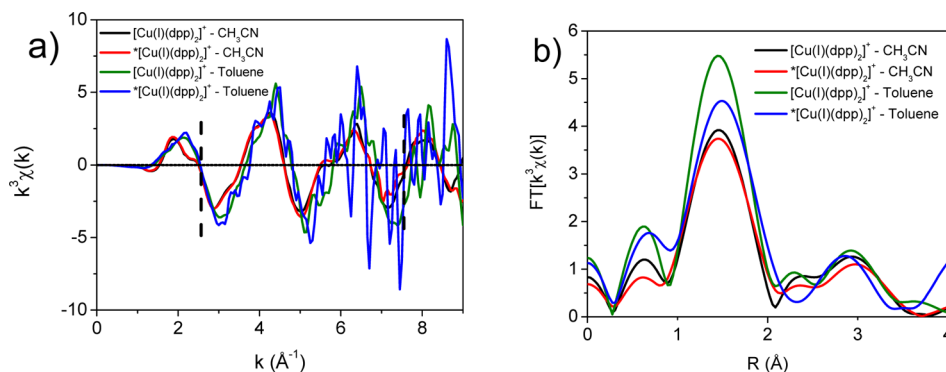
The excited-state dynamics of several copper phenanthrolines, in particular $[\text{Cu}(\text{I})(\text{dmp})_2]^+$, are known to be solvent dependent. Therefore, XTA measurements of $[\text{Cu}(\text{I})(\text{dpp})_2]^+$

Table 1. XAFS Fitting Parameters in Acetonitrile, with $S_0^2 = 1.0$, $\Delta E = 3 \text{ eV}^a$

atom–atom scattering path	atom–atom distances (Å) ($\pm 0.02 \text{ Å}$)			Debye–Waller factors (Å ²) ($\pm 0.001 \text{ Å}^2$)		
	[Cu(I)(dpp) ₂] ⁺	*[Cu(I)(dpp) ₂] ⁺	[Cu(II)(dpp) ₂] ²⁺	[Cu(I)(dpp) ₂] ⁺	*[Cu(I)(dpp) ₂] ⁺	[Cu(II)(dpp) ₂] ²⁺
Cu–N (CN = 4)	2.02	1.98	1.99	0.0076	0.0035	0.0064
Cu–C (b) (CN = 4)	2.76	2.78	2.75	0.0076	0.018	0.0067
Cu–C (c) (CN = 4)	3.02	2.98	3.00	0.0056	0.001	0.0029
Cu–C (d) (CN = 4)	3.25	3.15	3.16	0.0042	0.009	0.0087
Cu–C (e) (CN = 4)	3.31	3.27	3.27	0.001	0.001	0.002

^aEnergy shift between experimental and theoretical wavenumber grids.**Scheme 1. Atomic Centers Used in XAFS Data Fitting**

were performed in both coordinating acetonitrile and non-coordinating toluene solvents to determine if the MLCT state forms an “exciplex” with the solvent and if the structural dynamics of this bulky molecule exhibit any solvent dependence. Figure 6 shows the XANES spectra of the ground-state

**Figure 6.** Solvent-dependent XANES spectra of [Cu(I)(dpp)₂]⁺ and *[Cu(I)(dpp)₂]⁺ in both acetonitrile and toluene. The 527 nm excitation was used in both solvents. Percentage excited-state was determined in both solvents by linear combination fitting with [Cu(I)(dpp)₂]⁺ and [Cu(II)(dpp)₂]²⁺ spectra in acetonitrile.**Figure 7.** Solvent-dependent XAFS spectra, showing (a) k-space spectra and (b) R-space spectra of [Cu(I)(dpp)₂]⁺ and *[Cu(I)(dpp)₂]⁺ in acetonitrile and toluene, using Fourier transform with k range of 2.5–7.5 Å^{−1}.

and photoexcited sample in both toluene and acetonitrile. As stated earlier, the percentage excited-state for each photoexcited sample was determined by linear combination analysis using both the ground state [Cu(I)(dpp)₂]⁺ and [Cu(II)(dpp)₂]²⁺ in acetonitrile as standards. There are no noticeable differences between the XANES spectra in acetonitrile and toluene. In both solvents, the 1s → 4p_z is located at 8.986 keV, and the 1s → 3d peak appears in both photoexcited samples at 8.978 keV. Considering the long MLCT lifetime of about 100 ns in both solvents, it is likely that there is no strong coordination with either solvent due to the shielding of the two phenyl groups in the 2,9 position of phenanthroline that prohibit the access of the solvent molecules to the copper center. The XAFS spectra in k-space and the magnitude and imaginary functions in R-space after the Fourier Transformation for [Cu(I)(dpp)₂]⁺ and *[Cu(I)(dpp)₂]⁺ can be found in Figure 7. The fits in R-space can be found in Figure 8 and the results of the R-space fits in toluene are tabulated in Table 2.

3.3. DFT Calculations. DFT calculations were performed to determine the ground-state geometries of [Cu(I)(dpp)₂]⁺ and [Cu(II)(dpp)₂]²⁺, as well as the electronic and structural properties of *[Cu(I)(dpp)₂]⁺. The lowest lying excited ³[Cu(I)(dpp)₂]⁺ state calculated from TDDFT was chosen to model the excited state of interest in this work. The results are briefly summarized in Table 3; further information is provided in the Supporting Information. The DFT calculations indicate that the Cu–N distance decreases from 2.06 Å for [Cu(I)(dpp)₂]⁺ to 2.01 Å for excited ³[Cu(I)(dpp)₂]⁺ and [Cu(II)(dpp)₂]²⁺, while the angle between the two phenanthroline planes decreases by ~7°. The average Cu–N distance change in the MLCT state from that of the ground state is consistent with those determined by XTA. It should be noted that, while the flattening angle cannot be quantitatively determined using XAFS, the calculated flattening angle is rather small and consistent with the negligible change in intensity in the 1s→4p_z

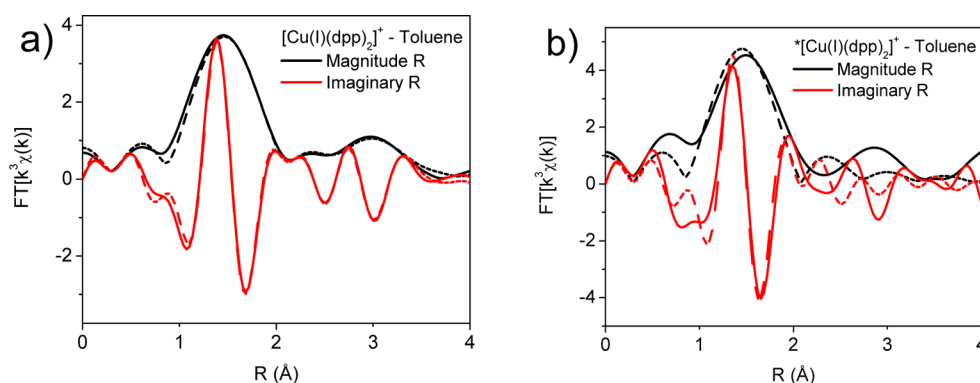


Figure 8. Magnitude and Imaginary R-space fits for (a) $[\text{Cu(I)(dpp)}_2]^+$ and (b) $*[\text{Cu(I)(dpp)}_2]^+$ in toluene. Due to poor signal-to-noise, only a first-shell fit was performed for $*[\text{Cu(I)(dpp)}_2]^+$. Ground-state was fit over range of 1–3.5 Å.

Table 2. XAFS Fitting Parameters in Toluene, with $S_0^2 = 1.0$, $\Delta E = 3 \text{ eV}^a$

atom–atom scattering path	atom–atom distances (Å) ($\pm 0.02 \text{ Å}$)		Debye–Waller factors (Å^2) ($\pm 0.001 \text{ Å}^2$)	
	$[\text{Cu(I)(dpp)}_2]^+$	$*[\text{Cu(I)(dpp)}_2]^+$	$[\text{Cu(I)(dpp)}_2]^+$	$*[\text{Cu(I)(dpp)}_2]^+$
Cu–N (CN = 4)	2.03	1.99	0.0083	0.0049
Cu–C (b) (CN = 4)	2.77		0.009	
Cu–C (c) (CN = 4)	3.00		0.001	
Cu–C (d) (CN = 4)	3.25		0.0046	
Cu–C (e) (CN = 4)	3.32		0.001	

^aEnergy shift between experimental and theoretical wavenumber grids.

Table 3. DFT Relevant Parameters (Angles in Degrees, Distances in Å)

	$[\text{Cu(I)(dpp)}_2]^+$	$[\text{Cu(II)(dpp)}_2]^{2+}$	$*[\text{Cu(I)(dpp)}_2]^+$
Cu–N (Å)	2.061	2.008	2.019
Cu–N–Cu angle (interphenanthroline)	114.8	110.1	110.9
Cu–N–Cu angle (intraphenanthroline)	82.4	83.8	83.3
phenyl–phenanthroline dihedral angle	40.7	43.6	42.5
phenanthroline–phenanthroline flattening angle	69.4	61.9	62.7

peak in the XANES region between $[\text{Cu(II)(dpp)}_2]^+$ and $*[\text{Cu(I)(dpp)}_2]^+$.

Figure 9 shows the calculated frontier orbital structure of $[\text{Cu(I)(dpp)}_2]^+$ in the relaxed lowest excited triplet state geometry (oscillator strength and symmetries are in the Supporting Information), corresponding to a $d_{xz} \rightarrow \pi^*$ transition. In the ground state, the electron density is located around the copper and nitrogen atoms; upon excitation in the MLCT band, the electron density is shifted onto the phenanthroline ligands. Because the phenyl rings are rotated $\sim 40^\circ$ out of plane with the phenanthroline ligands in the excited state, there is no additional electron density transferred on to the phenyl groups as a result of the MLCT transition. Instead, the transferred electron density remains localized on the phenanthroline ligands. The ramifications of this will be discussed below. It is important to note that DFT calculations poorly model the phenyl ring rotation even with an empirical

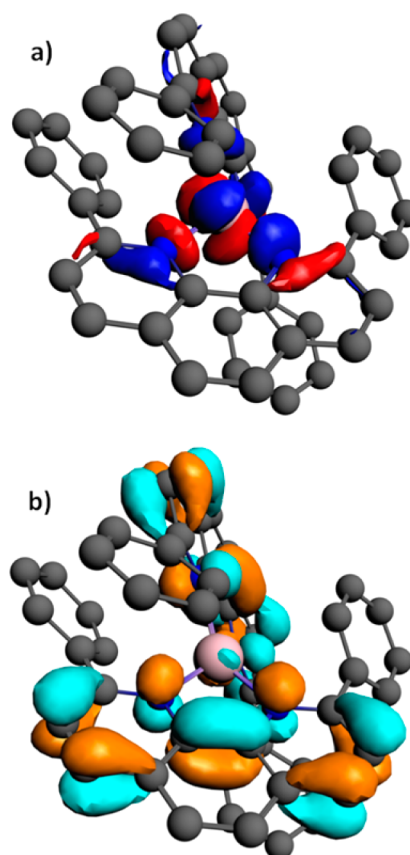


Figure 9. (a) HOMO and (b) LUMO of $[\text{Cu(I)(dpp)}_2]^+$ in the relaxed triplet geometry. Calculation of the lowest lying singlet–triplet transition in the relaxed geometry showed the excited $^3[\text{Cu(I)(dpp)}_2]^+$ state to be predominantly (97%) HOMO \rightarrow LUMO in character, after projection of the excited state spin density onto the ground state orbitals. This renders the LUMO orbital a good approximation to the excited state electronic wave function. The lowest triplet state (1.5635 eV) with B_2 symmetry was optimized. The isodensity cutoff for the orbital surfaces was 0.03 e/bohr.³ Orbitals were visualized with ADFView.

dispersion correction. The measured Cu–C(d) distance measured in the XTA measurements actually suggests a phenyl–phenanthroline dihedral angle decrease of $\sim 10^\circ$ in the excited state. However, such a small deviation likely will not have a significant effect on the distribution of electron density in the excited state and as such the plots of Figure 9 are reliable.

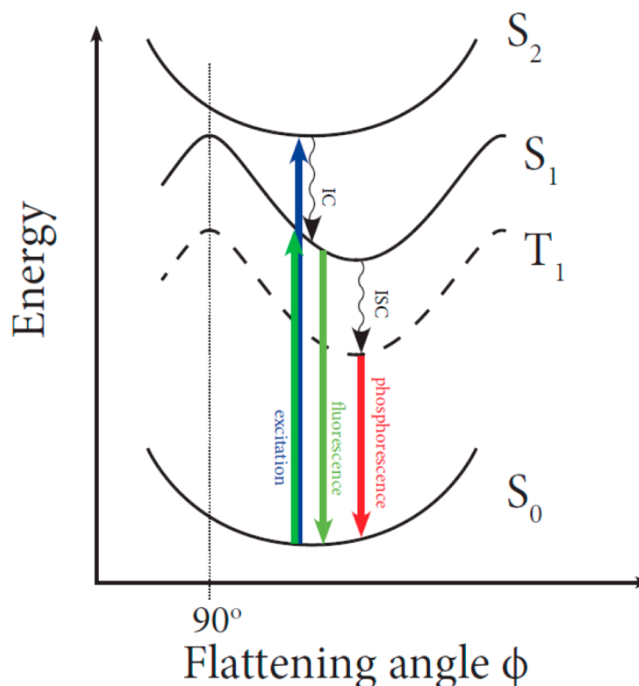
4. DISCUSSION

4.1. $[\text{Cu}(\text{I})(\text{dpp})_2]^+$ Adopts a Flattened Ground-State Structure in Solution. It is well-known that $[\text{Cu}(\text{I})(\text{dmp})_2]^+$ has a pseudotetrahedral coordination geometry of the copper center with a D_{2d} symmetry in the ground state.^{18,37,62} As a result, the UV–vis spectrum exhibits strong absorption around 435 nm corresponding to the symmetry-allowed $S_2 \leftarrow S_0$ transition,^{18,34,36,38} and a very weak shoulder feature to the red corresponding to the small population of the dynamically flattened tetrahedral geometry that has been shown to allow the symmetry-forbidden $S_1 \leftarrow S_0$ transition. The UV–vis spectrum of $[\text{Cu}(\text{I})(\text{dpp})_2]^+$ exhibits a pronounced red shoulder, signifying a strong $S_1 \leftarrow S_0$ transition and suggesting a significantly flattened ground state. It has been shown that $[\text{Cu}(\text{I})(\text{dtbp})_2]^+$ (dtbp, di-*tert*-butyl-phenanthroline), perhaps the most sterically hindered 2,9-substituted copper bisphenanthroline, is forced into an almost perfectly tetrahedral geometry due to the large size of the bulky *tert*-butyl ligands.⁴⁰ As such, this complex exhibits virtually no absorption into the $S_1 \leftarrow S_0$ band and therefore no shoulder at redder wavelengths. However, in an aryl-substituted complex like $[\text{Cu}(\text{I})(\text{dpp})_2]^+$, the aromatic phenyl groups on one hand hinder the pseudotetrahedral coordination geometry, and on the other hand are capable of π – π stacking interactions with the opposite phenanthroline ligand that stabilizes the ground state with flattened tetrahedral coordination geometry. The molecule flattens to accommodate this stabilizing interaction, breaking the D_{2d} symmetry and leading to a more allowed $S_1 \leftarrow S_0$ transition.⁴² One may also question the effect of potentially larger conjugated ligands of dpp vs dmp which could contribute to the red-shifted and enhanced absorption. However, this possibility was mostly ruled out based on our previous studies on $\text{Cu}(\text{I})$ bis(3,8-di(ethynyltrityl)-1,10-phenanthroline), $[\text{Cu}^{\text{I}}(\text{detp})_2]^+$ where the ligand conjugation was extended via the substituents at 3,8-positions of the 1,10-phenanthroline while no substituent groups other than hydrogens are at the 2,9 positions.²⁴ Although $[\text{Cu}^{\text{I}}(\text{detp})_2]^+$ displays an overall red-shift in the UV/vis spectrum at the main peak and shoulder features compared to that of $[\text{Cu}^{\text{I}}(\text{dmp})_2]^+$, the relative intensity ratio of the two absorption features resembles that in $[\text{Cu}^{\text{I}}(\text{phen})_2]^+$. Therefore, it is the angle between the two phenanthroline planes that controls the growth of the shoulder feature in the absorption spectra. From a light harvesting stand point, $[\text{Cu}(\text{I})(\text{dpp})_2]^+$ is a better candidate than $[\text{Cu}(\text{I})(\text{dmp})_2]^+$ in large part due to its enhanced shoulder absorption feature enabling an increased spectral overlap with the solar spectrum.

The XAFS spectra of the ground and photoexcited $[\text{Cu}(\text{I})(\text{dpp})_2]^+$ further indicate significant ground state flattening, as the edge peak corresponding to a $1s \rightarrow 4p_z$ transition is much more intense than that in $[\text{Cu}(\text{I})(\text{dmp})_2]^+$ and retains approximately equal intensity in the ground and excited states. The DFT calculations suggest that $[\text{Cu}(\text{I})(\text{dpp})_2]^+$ adopts a 69° flattening angle in the ground state and flattens further to 62° upon photoexcitation. Such a flattening distortion was predicted by TA measurements, which observed a subpicosecond rise time¹⁶ in the excited state absorption feature which has previously been assigned as the time constant for the flattening due to the pseudo Jahn–Teller distortion.^{18,40} While steric effects and the interligand phenyl-phenanthroline interactions force $[\text{Cu}(\text{I})(\text{dpp})_2]^+$ to adopt a flattened ground-state geometry, Jahn–Teller distortions caused by vacating the

$\text{Cu } d_{xz}$ orbital still drive further flattening in the MLCT excited state. A potential energy diagram describing the flattening distortions in the ground and excited states was constructed (Scheme 2) using the structural analysis from XAFS measure-

Scheme 2. Potential Energy Diagram for $[\text{Cu}(\text{I})(\text{dpp})_2]^+$ As a Function of Phenanthroline Flattening Angle^a



^aElectronic dynamics determined from transient absorption measurements were previously published.¹⁶

ments and previously published TA measurements.¹⁶ It should be noted that there is an energy maximum at a phenanthroline–phenanthroline angle of 90° (D_{2d} symmetry) for the Jahn–Teller distorted S_1 and T_1 states because the $3d^9$ copper center prefers a 5-coordinate geometry.

4.2. Solvent-Independent MLCT State Dynamics in $[\text{Cu}(\text{I})(\text{dpp})_2]^+$. As a result of the transient $\text{Cu}(\text{II})$ species ($3d^9$) generated via the MLCT transition, some $\text{Cu}(\text{I})$ diimine complexes are susceptible to the solvent quenching of the excited-state.³⁷ It has been shown that $[\text{Cu}(\text{I})(\text{phen})_2]^+$ is nonemissive with a very short MLCT state lifetime, even in a noncoordinating solvent such as dichloromethane²⁴ and at cryogenic temperatures.⁴ Also, optical TA and XTA measurements have shown strong solvent dependent MLCT dynamics of $[\text{Cu}(\text{I})(\text{dmp})_2]^+$.^{16,37} Time-resolved emission results suggest that $[\text{Cu}(\text{I})(\text{dmp})_2]^+$ exhibits a fast, nonradiative decay to the ground state in solvents such as acetonitrile, but exhibits a nanosecond, high quantum yield emission in noncoordinating solvents, such as toluene.^{4,23} The properties of these two complexes are rationalized by considering the availability of open avenues by which the solvent might access the photogenerated $\text{Cu}(\text{II})$ center. In $[\text{Cu}(\text{I})(\text{phen})_2]^+$ and $[\text{Cu}^{\text{I}}(\text{detp})_2]^+$,²⁴ where only H-atoms are at the 2,9 positions of the phenanthroline ligands, it is easy for solvents to approach the copper center to lower the energy of the MLCT state, and consequently quench the MLCT state through nonradiative pathways according to the energy gap law.⁴ In comparison, the copper center in $[\text{Cu}(\text{I})(\text{dmp})_2]^+$ is better protected due to the

methyl groups, and as such only strongly coordinating solvents successfully quench this complex. The XAFS spectra of $[\text{Cu}(\text{I})(\text{dpp})_2]^+$ shown in Figure 6 show that there is no appreciable change between $[\text{Cu}(\text{I})(\text{dpp})_2]^+$ in either toluene or acetonitrile, both in the ground state and 100 ps following excitation. The first shell fits for $*[\text{Cu}(\text{I})(\text{dpp})_2]^+$ reveal a Cu–N coordination of 4 and the same Cu–N distance both in acetonitrile and toluene, proving that the excited-state structure of this complex is solvent-independent. It is clear that switching from methyl groups to much bulkier phenyl groups at the 2,9 positions of the phenanthroline provides sufficient protection to the copper center to prevent exciplex formation on the ultrafast time scale. A copper system protected from exciplex formation is ideal for use in solar energy applications for two reasons. First, if solvent binding occurs on the time scale of electron injection into the acceptor material, then solvent ligation could quench some of the copper molecules and prevent electron transfer. Second, lowering the total energy of the system via exciplex formation could make the complex more vulnerable to charge recombination, essentially resulting in a wasted photon. As such, it is evident that the solvent independent dynamics of $[\text{Cu}(\text{I})(\text{dpp})_2]^+$ are well suited to solar energy applications, which has been demonstrated by our recent study of its sulfonate derivative in mimicking a DSSC.⁶⁶

4.3. The Localization of the MLCT State of $*[\text{Cu}(\text{I})(\text{dpp})_2]^+$ on the Phenanthrolines. In the MLCT state of $[\text{Cu}(\text{I})(\text{phen})_2]^+$, the *d*-electron from the copper center is primarily localized on a single phenanthroline ligand; when aryl groups are added to the 2,9 positions of the phenanthroline ligand, the charge in the MLCT state could further delocalize beyond the phenanthroline ligands.³⁵ In a system with aryl substitutions at the 2,9 positions of the phenanthroline ligand, such as $[\text{Cu}(\text{I})(\text{dpp})_2]^+$, the ligand charge could further delocalize over the phenyl groups if there are strong π – π interactions between the phenyl and opposite phenanthroline, or if there was sufficient conjugation between the phenyl rings and the corresponding phenanthroline ligand. The rational design of a copper complex for solar energy applications requires explicit knowledge of how charge is distributed in the MLCT state, such as the linker positions for anchoring the transition metal complex sensitizers to the TiO_2 nanoparticle surfaces.¹⁴

Although both $*[\text{Cu}(\text{I})(\text{dpp})_2]^+$ and $[\text{Cu}(\text{II})(\text{dpp})_2]^{2+}$ have a nominally Cu(II) center, their total electron densities are different. The former has more electron density on the ligands than the latter. It is important to note that the average Cu–N, Cu–C(d), and Cu–C(e) distances of these two systems are identical within the experimental precisions of 0.02 Å for XAFS measurements. The crystal structure of $[\text{Cu}(\text{II})(\text{dpp})_2]^{2+}$ indicates that the phenyl rings no longer maintain a significant π interaction with the opposite phenanthroline ligand in this oxidized complex.⁴² However, these phenyl rings are not coplanar with the phenanthroline ligands either. One expected route for stabilizing the MLCT excited state could be the distribution of the electron across the π^* orbital of the phenyl rings, lowering the total energy of the system. However, since the rotation of the phenyl ring is quite similar between $*[\text{Cu}(\text{I})(\text{dpp})_2]^+$ and $[\text{Cu}(\text{II})(\text{dpp})_2]^{2+}$, the phenyl ring is still too far out of plane with the phenanthroline to allow appreciable delocalization across the phenyls. The calculated spin density of the lowest-lying excited $^3[\text{Cu}(\text{I})(\text{dpp})_2]^+$ state in the relaxed excited-state geometry was determined, after projection onto the frontier orbitals of the ground state

complex, to resemble a HOMO to LUMO transition (97% weighting). Figure 9 presents the ground state HOMO and LUMO that characterize the transition being modeled (Additional information is provided in the Supporting Information). It is clearly shown in Figure 9 that in the MLCT state, the electron density is located entirely on the phenanthroline ligands and not on the phenyl rings. Thus, none of the electron density transferred from the copper center ends up on the phenyl rings in the relaxed triplet state. Furthermore, if there was significant electron density distributed through the phenyl π^* orbitals, one would expect some structural distortion in the phenyl rings, which would likely manifest as an increase in the Debye–Waller factor associated with paths (d) and (e); the Cu–C distances of paths (d) and (e) and the Debye–Waller factors associated with path (e) are the same within error between $*[\text{Cu}(\text{I})(\text{dpp})_2]^+$ and $[\text{Cu}(\text{II})(\text{dpp})_2]^{2+}$, indicating that no structural distortion is caused by the extra electron density. However, the Debye–Waller factor associated with path (b) of $*[\text{Cu}(\text{I})(\text{dpp})_2]^+$ is much larger than those for path (b) of the ground or oxidized state complexes, indicating significant deformation in the interior of the phenanthroline ligands. As such, the XAFS measurements are consistent with a deformation of the phenanthroline ligands in the excited state as a result of an additional localized charge on the phenanthroline and therefore corroborate the DFT calculations. Both the experimental and computational results indicate that the phenyl rings do not see any of the electron density from the copper center in the MLCT state; instead, all of the electron density is centered on the phenanthroline ligands.

The previous results could have significant ramifications on the use of aryl-substituted copper bisphenanthroline complexes in solar energy conversion devices. In a DSSC, the copper complex needs to effectively transfer an electron into a semiconductor nanoparticle. It is important that the copper complex is lined up properly next to the semiconductor surface such that, upon photoexcitation, there is significant electron density close enough to the semiconductor to quickly transfer via either a hopping or tunneling mechanism. We have observed highly efficient electron injection into TiO_2 from a sulphonated $[\text{Cu}(\text{I})(\text{dpp})_2]^+$ complex.⁶⁶ This system had phenyl groups sulfonated at the meta and para positions, making the complex water-soluble and allowing it to stick electrostatically to TiO_2 nanoparticles. Such a system could orient itself in such a way to optimize electron injection into the TiO_2 ; however, a chemisorbed copper system must be rationally designed to strictly enforce an effective electron injection orientation. While it is unknown what orientation is optimal for electron transfer, these results seem to indicate that binding to TiO_2 via substituents at the 2,9 positions would likely be ineffective, since the majority of electron density in the MLCT state is heavily localized near the center of the phenanthroline. Instead, perhaps a more effective approach would be substitutions at the 4,7 or 5,6 positions. In particular, additional phenyl substitutions at the 4,7 positions have been shown to nearly double the maximum extinction coefficient relative to those complexes with only substitutions at the 2,9 positions.⁶¹ Thus, a system designed in this way could not only function as a better solar radiation harvester, but might also exhibit improved electron injection in TiO_2 , resulting in a very effective sensitizer dye.

5. CONCLUSIONS

The photoinduced structural changes of the $[\text{Cu}(\text{I})(\text{dpp})_2]^+$ MLCT state were measured both in acetonitrile and toluene using X-ray transient absorption spectroscopy and calculated by density functional theory. $[\text{Cu}(\text{I})(\text{dpp})_2]^+$ exhibited no photo-initiated exciplex formation in acetonitrile, maintaining the same Cu–N distance in both acetonitrile and toluene. Upon excitation, $^*[\text{Cu}(\text{I})(\text{dpp})_2]^+$ exhibits a subpicosecond pseudo Jahn–Teller flattening distortion, followed by electron transfer to the phenanthroline ligands. The photoexcited species has a nominally Cu(II) center with a structure quite similar to that of the fully oxidized $[\text{Cu}(\text{II})(\text{dpp})_2]^{2+}$ species, the only exception being distortions on the phenanthroline ligand due to the additional charge provided by the transferred electron. The phenyl rings at the 2,9 positions rotate from their initial positions upon excitation, breaking the stabilizing π -stacking interaction. However, the phenyl rings never rotate back into plane with the phenanthroline ligands, resulting in poor conjugation between the phenyl rings and the phenanthroline ligands. The phenyl rings are oriented such that they provide excellent shielding of the copper center, protecting it from solvent attack and extending the MLCT lifetime in coordinating solvents. The protective ability of the phenyl rings results in solvent-independent dynamics that are not exhibited in $[\text{Cu}(\text{I})(\text{dmp})_2]^+$. However, the phenyl rings do not carry an appreciable amount of the additional charge in the excited state; this fact could have significant implications in the design of copper-based sensitizer dyes in DSSCs.

■ ASSOCIATED CONTENT

■ Supporting Information

Linear combination fits of standard $[\text{Cu}(\text{I})(\text{dpp})_2]^+$ and $[\text{Cu}(\text{II})(\text{dpp})_2]^{2+}$ to transient XAFS spectra, synthesis and NMR characterization of $[\text{Cu}(\text{I})(\text{dpp})_2]^+$ and $[\text{Cu}(\text{II})(\text{dpp})_2]^{2+}$. Geometry optimization results from TD-DFT calculations, lowest singlet and triplet-excited state energies and symmetries, and calculated MLCT absorption spectrum. This material is available free of charge via the Internet at <http://pubs.acs.org>.

■ AUTHOR INFORMATION

Corresponding Author

*Phone: 630-252-3533 or 847-491-3479; e-mail: lchen@anl.gov or l-chen@northwestern.edu.

Notes

The authors declare no competing financial interest.

■ ACKNOWLEDGMENTS

The work was supported by the U.S. Department of Energy, Office of Science, Office of Basic Energy Sciences, under Contract No. DE-AC02-06CH11357. Use of the Advanced Photon Source at Argonne National Laboratory was supported by the U.S. Department of Energy, Office of Science, Office of Basic Energy Sciences, under Contract No. DE-AC02-06CH11357. N.E.J. thanks the NSF for the award of Graduate Research Fellowship (NSF DGE-0824162). The authors would like to thank Dr. Klaus Attenkofer of the Advanced Photon Source for their help with the XTA experiment.

■ REFERENCES

- (1) Grätzel, M. J. *Photochem. Photobiol. C: Photochem. Rev.* **2003**, *4*, 145–153.
- (2) Nazeeruddin, M. K.; Grätzel, M. *Struct. Bonding (Berlin)* **2007**, *123*, 113–175.
- (3) McCusker, J. K. *Acc. Chem. Res.* **2003**, *36*, 876–887.
- (4) McMillin, D. R.; Kirchoff, J. R.; Goodwin, K. V. *Coord. Chem. Rev.* **1985**, *64*, 83–92.
- (5) Ruthkosky, M.; Kelly, C. A.; Castellano, F. N.; Meyer, G. J. *Coord. Chem. Rev.* **1998**, *171*, 309–322.
- (6) Lavie-Combote, A.; Cantuel, M.; Leydet, Y.; Jonusauskas, G.; Bassani, D. M.; McClenaghan, N. D. *Coord. Chem. Rev.* **2008**, *252*, 2572–2584.
- (7) Gray, H. B.; Maverick, A. W. *Science* **1981**, *214*, 1201–1205.
- (8) Smith, C. S.; Mann, K. R. *Chem. Mater.* **2009**, *21*, S042–S049.
- (9) Benedict, J. B.; Coppens, P. J. *Am. Chem. Soc.* **2010**, *132*, 2938–2944.
- (10) Mutofin, S.; Chan, E. J.; Healy, P. C.; Marinnelli, A.; Ngoune, J.; Pettinari, C.; Pettinari, R.; Somers, N.; Skelton, B. W.; White, A. H. *Inorg. Chim. Acta* **2008**, *361*, 2365–2374.
- (11) Fry, H. C.; Lucas, H. R.; Sarjeant, A. A. N.; Karlin, K. D.; Meyer, G. J. *Inorg. Chem.* **2008**, *47*, 241–256.
- (12) Lenzmann, F. O.; Kroon, J. M. *Adv. Optoelectronics* **2007**, 1–10.
- (13) Paris, J. P.; Brandt, W. W. *J. Am. Chem. Soc.* **1959**, *81*, 5001–5002.
- (14) Bessho, T.; Constable, E. C.; Graetzel, M.; Hernandez Redondo, A.; Housecroft, C. E.; Kylberg, W.; Nazeeruddin, M. K.; Neuburger, M.; Schaffner, S. *Chem. Commun.* **2008**, 3717–3719.
- (15) Armaroli, N.; Accorsi, G.; Cardinali, F.; Listorti, A. *Top. Curr. Chem.* **2007**, *280*, 69–115.
- (16) Shaw, G. B.; Grant, C. D.; Shirota, H.; E. W., C., Jr.; Meyer, G. J.; Chen, L. X. *J. Am. Chem. Soc.* **2007**, *129*, 2147–2160.
- (17) Rorabacher, D. B. *Chem. Rev.* **2004**, *104*, 651–698.
- (18) Iwamura, M.; Takeuchi, S.; Tahara, T. *J. Am. Chem. Soc.* **2007**, *129*, S248–S256.
- (19) Patterson, G. S.; Holm, R. H. *Bioinorg. Chem.* **1975**, *4*, 257–275.
- (20) Kirchoff, J. R.; Roland E. Gamache, J.; Blaskie, M. W.; Paggio, A. A. D.; Legel, R. K.; McMillin, D. R. *Inorg. Chem.* **1983**, *22*, 2380–2384.
- (21) Samia, A. C. S.; Cody, J.; Fahrni, C. J.; Burda, C. J. *Phys. Chem. B* **2004**, *108*, S63–S69.
- (22) Gunaratne, T.; Rodgers, M. A. J.; Felder, D.; Nierengarten, J.-F.; Accorsi, G.; Armaroli, N. *Chem. Commun.* **2003**, 3010–3011.
- (23) Blaskie, M. W.; McMillin, D. R. *Inorg. Chem.* **1980**, *19*, 3519–3522.
- (24) Lockard, J. V.; Kabehie, S.; Zink, J. I.; Smolentsev, G.; Soldatov, A.; Chen, L. X. *J. Phys. Chem. B* **2010**, *114*, 14521–14527.
- (25) Ruthkosky, M.; Castellano, F. N.; Meyer, G. J. *Inorg. Chem.* **1996**, *35*, 6406–6412.
- (26) Berger, R. M.; McMillin, D. R.; Dallinger, R. F. *Inorg. Chem.* **1987**, *26*, 3802–3805.
- (27) Cuttell, D. G.; Kuang, S.-M.; Fanwick, P. E.; McMillin, D. R.; Walton, R. A. *J. Am. Chem. Soc.* **2002**, *124*, 6–7.
- (28) Miller, M. T.; Gantzel, P. K.; Karpishin, T. B. *J. Am. Chem. Soc.* **1999**, *121*, 4292–4293.
- (29) Kober, E. M.; Caspar, J. V.; Lumpkin, R. S.; Meyer, T. J. *J. Phys. Chem.* **1986**, *90*, 3722–3734.
- (30) Meyer, T. J. *Acc. Chem. Res.* **1989**, *22*, 163–170.
- (31) Scaltrito, D. V.; Thompson, D. W.; O'Callaghan, J. A.; Meyer, G. J. *Coord. Chem. Rev.* **2000**, *208*, 243–266.
- (32) Miller, M. T.; Gantzel, P. K.; Karpishin, T. B. *Inorg. Chem.* **1999**, *38*, 3414.
- (33) Miller, M. T.; Karpishin, T. B. *Inorg. Chem.* **1999**, *38*, S246–S249.
- (34) Zgierski, M. Z. *J. Chem. Phys.* **2003**, *118*, 4045–4051.
- (35) Wang, X.; Wang, W.; Koyama, M.; Kubo, M.; Miyamoto, A. *J. Photochem. Photobiol. A: Chem.* **2006**, *179*, 149–155.
- (36) Siddique, Z. A.; Yamamoto, Y.; Ohno, T.; Nozaki, K. *Inorg. Chem.* **2003**, *42*, 6366–6378.
- (37) Chen, L. X.; Shaw, G. B.; Novozhilova, I.; Liu, T.; Jennings, G.; Attenkofer, K.; Meyer, G. J.; Coppens, P. J. *Am. Chem. Soc.* **2003**, *125*, 7022–7034.

- (38) Iwamura, M.; Watanabe, H.; Ishii, K.; Takeuchi, S.; Tahara, T. *J. Am. Chem. Soc.* **2011**, *133*, 7728–7736.
- (39) Chen, L. X.; Jennings, G.; Liu, T.; Gosztola, D. J.; Hessler, J. P. *J. Am. Chem. Soc.* **2002**, *124*, 10861–10867.
- (40) Gothard, N. A.; Mara, M. W.; Huang, J.; Szarko, J. M.; Rolczynski, B.; Lockard, J. V.; Chen, L. X. *J. Phys. Chem. A* **2012**, *116*, 1984–1992.
- (41) Phifer, C. C.; McMillin, D. R. *Inorg. Chem.* **1986**, *25*, 1329–1333.
- (42) Miller, M. T.; Gantzel, P. K.; Karpishin, T. B. *Inorg. Chem.* **1998**, *37*, 2285–2290.
- (43) Harpham, M. R.; Nguyen, S. C.; Hou, Z.; Grossman, J. C.; Harris, C. B.; Mara, M. W.; Stickrath, A. B.; Kanai, Y.; Kolpak, A. M.; Lee, D.; et al. *Angew. Chem., Int. Ed.* **2012**, *51*, 7692–7696.
- (44) Chen, L. X. *Annu. Rev. Phys. Chem.* **2005**, *56*, 221–254.
- (45) Chen, L. X. *J. Electron Spectrosc. Relat. Phenom.* **2001**, *119*, 161–174.
- (46) Newville, M. *J. Synchrotron Radiat.* **2001**, *8*, 322–324.
- (47) Ravel, B.; Newville, M. *J. Synchrotron Radiat.* **2005**, *12*, 537–541.
- (48) Newville, M.; Liviš, P.; Yacoby, Y.; Rehr, J. J.; Stern, E. A. *Phys. Rev. B* **1993**, *47*, 14126–14131.
- (49) Lytle, F. W.; Sayers, D. E.; Stern, E. A. *Phys. Rev. B* **1975**, *11*, 4825–4835.
- (50) Stern, E. A.; Sayers, D. E.; Lytle, F. W. *Phys. Rev. B* **1975**, *11*, 4836–4846.
- (51) Sayers, D. E.; Stern, E. A.; Lytle, F. *Phys. Rev. Lett.* **1971**, *27*, 1204–1207.
- (52) Bunker, G. *Introduction to XAFS: A Practical Guide to X-ray Absorption Fine Structure Spectroscopy*; Cambridge University Press: United Kingdom, 2010.
- (53) te Velde, G.; Bickelhaupt, F. M.; Baerends, E. J.; Fonseca Guerra, C.; van Gisbergen, S. J. A.; Snijders, J. G.; Ziegler, T. *J. Comput. Chem.* **2001**, *22*, 931–967.
- (54) Fonseca Guerra, C.; Snijders, J. G.; te Velde, G.; Baerends, E. J. *Theor. Chem. Acc.* **1998**, *99*, 391–403.
- (55) ADF2012, SCM, *Theoretical Chemistry*; Vrije Universiteit: Amsterdam, The Netherlands, <http://www.scm.com>.
- (56) Lenthe, E. v.; Baerends, E. J.; Snijders, J. G. *J. Chem. Phys.* **1993**, *99*, 4597–4610.
- (57) Lenthe, E. v.; Baerends, E. J.; Snijders, J. G. *J. Chem. Phys.* **1994**, *101*, 9783–9792.
- (58) van Lenthe, E.; van Leeuwen, R.; Baerends, E. J.; Snijders, J. G. *Int. J. Quantum Chem.* **1996**, *57*, 281–293.
- (59) Grimme, S.; Antony, J.; Ehrlich, S.; Krieg, H. *J. Chem. Phys.* **2010**, *132*, 154104.
- (60) Chang, C.; Pelissier, M.; Durand, P. *Phys. Scr.* **1986**, *34*, 394.
- (61) Armaroli, N. *Chem. Soc. Rev.* **2001**, *30*, 113–124.
- (62) Hamalainen, R.; Ahlgren, M.; Turpeinen, U.; Raikas, T. *Cryst. Struct. Comm.* **1979**, *8*, 75–80.
- (63) Kau, L. S.; Spira-Solomon, D. J.; Penner-Hahn, J. E.; Hodgson, K. O.; Solomon, E. I. *J. Am. Chem. Soc.* **1987**, *109*, 6433–6442.
- (64) Smith, T. A.; Penner-Hahn, J. E.; Berding, M. A.; Doniach, S.; Hodgson, K. O. *J. Am. Chem. Soc.* **1985**, *107*, S945–S955.
- (65) Zabinsky, S. I.; Rehr, J. J.; Ankudinov, A.; Albers, R. C.; Eller, M. *J. Phys. Rev. B* **1995**, *52*, 2995–3009.
- (66) Huang, J.; Buyukcakil, O.; Mara, M. W.; Coskun, A.; Dimitrijevic, N. M.; Barin, G.; Kokhan, O.; Stickrath, A. B.; Ruppert, R.; Tiede, D. M.; et al. *Angew. Chem.* **2012**, *51*, 12711–12715.